

Self-Organized Oxide Nanotube Layers on Titanium and Other Transition Metals

P. Schmuki

1 Introduction

Self-organized nanostructures of different metals or semiconductors have received considerable attention due to the anticipated high technological potential of these materials. For Al it is long known that anodization in various solutions leads to the formation of ordered porous oxide layers [1–4]. Since the remarkable work of Masuda et al. [1], it is clear that very high degree of order can be achieved with these porous geometries. Many applications of these ordered alumina structures have been shown, for example, using it as a photonic crystal [5], or as a template for the deposition of other materials [6–8]. For a range of other metals such as Ti [9–17], Zr [18–20], Nb [21], W [22, 23], Ta [24, 25], Hf [26], it has recently been found that self-organized porous structures can be formed under optimized electrochemical treatments. Figure 1 shows examples of nanotubular structures produced on Ti and other transition metals. These nanoarchitected oxide films can have very specific functional properties. For example, nanotubes made of titanium oxide (TiO_2) combine geometrical advantages given by their array structure with the material specific properties of TiO_2 . Titanium oxide is used in functional applications such as self-cleaning surfaces [27] and solar cell applications [28], or explored for gas-sensing capabilities [29].

Particular advantages of regular tube arrays as shown in Fig. 1 are the large surface area and the defined geometry. The defined geometry results in a narrow distribution of diffusion path not only for entering the tubular depth (e.g., reactants to be transported to the tube bottom) but also for species to be transported through the tube wall, for example, electrons, holes, and ions. Therefore, the system response of ordered tube arrays in applications such as sensing or photocatalysis is expected to be much more defined than using classical high surface area layers – for example,

P. Schmuki (✉)

University of Erlangen-Nuremberg, Department of Materials Science, LKO, Martensstrasse 7,
D-91058 Erlangen, Germany
e-mail: schmuki@ww.uni-erlangen.de

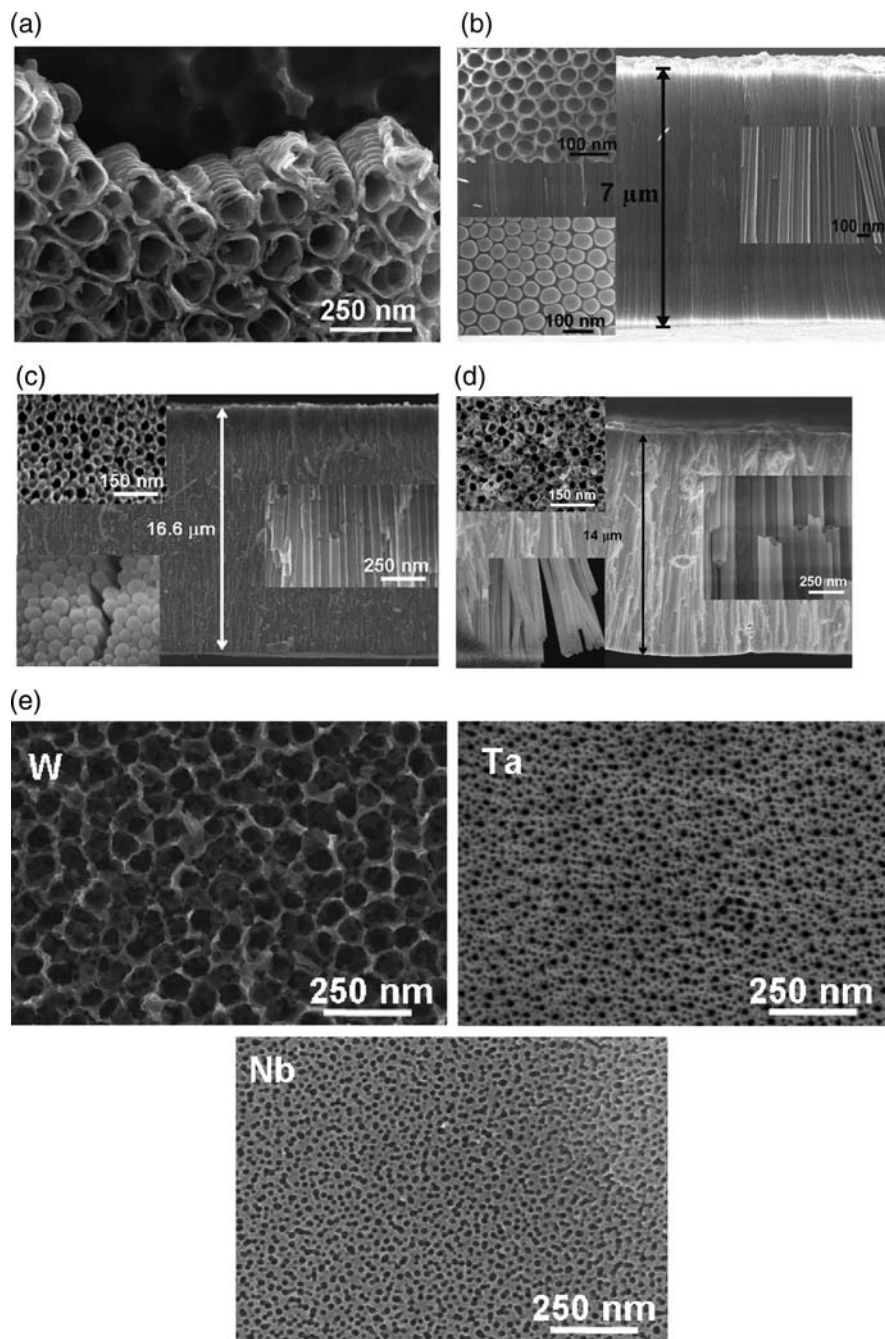


Fig. 1 SEM images showing morphology of various transition metal oxide nanotube layers produced by anodization in fluoride-containing solutions; TiO₂ (a, b), ZrO₂ (c), HfO₂ (d), WO₃ + Ta₂O₅ + Nb₂O₅ (e); insets show top views (*open tubes*) and bottom views (*closed ends*) and side walls in detail

layers where nanoparticles are compacted or sintered to produce an open porous network.

Ordered nanotubular structures of TiO_2 and other transition metal oxides have been formed by electrochemical anodization of the metal in electrolytes containing small amounts of hydrofluoric acid (HF). In general, the morphology and the structure of porous layers are affected strongly by the electrochemical and the solution parameters. Under optimized conditions self-organized highly ordered nanotubes with a length between some few 10 nm and several 100 μm are formed consisting of arrays with single tube diameter between 10 and 100 nm and a tube wall of some 10 nm thickness. The present chapter discusses factors of the electrochemical pore-formation process and key electrochemical parameters that lead to the formation of these self-organized structures, as well as some properties that can be exploited in various applications.

2 Overview on the Electrochemistry of Valve Metals

For the oxide structures shown in Fig. 1, the base metals (Ti, W, Zr, Hf, Ta, Nb) belong to the class of so-called valve metals. In contrast to other metals, on valve metals it is possible to grow compact oxide layers of considerable thickness (some 100 nm) in aqueous electrolytes. Anodization of valve metals has been widely investigated in a variety of acids at voltages typically up to several hundreds volts. Up to a voltage, where dielectric breakdown of certain spots of an oxide layer occurs, a uniform and compact layer of TiO_2 can be obtained (see e.g., Refs. [30–32] and references therein). For oxide films formed below the breakdown voltage, typically a growth rate of 1–5 nm/V has been reported [33, 34]. A selection of properties of anodic valve metal oxides has been compiled in Table 1. It is apparent that the structural, electronic, and ionic properties cover a wide range. Looking at the electronic properties, that is, from the relatively well-conducting SnO_2 over the semiconductive oxides TiO_2 , ZnO , WO_3 to insulating ZrO_2 , HfO_2 , Al_2O_3 . The growth mechanism can be completely dominated by anion inward transport (ZrO_2 , HfO_2) to cases with considerable cation outward contribution (Al_2O_3). Also remarkable is that the structure of the grown oxide can be amorphous or crystalline. However, the morphology, structure (and the maximum achievable thickness) of anodic oxide layers formed on valve metals strongly depends on the specific electrochemical parameters such as the applied potential, the time of anodization, or the sweep rate of the potential ramp. For example, the structure of the oxide films on Ti has typically been reported to be amorphous at low voltages (below 20 V [31]), and crystallization to take place at higher voltages. Depending on the anodizing conditions, the crystal structure has been reported to be anatase [33, 34–37], a mixture of anatase and rutile [33, 37, 38], or rutile [33, 37].

At comparably high voltages, if a sufficient electric field is applied to an oxide film, dielectric breakdown (by a Zener or avalanche mechanism) will take place [33, 38]. This is apparent in I – U curves by a rapid current increase, at a distinct breakdown voltage U_{bd} [39–43], or by current or potential fluctuations. Breakdown events can become apparent by sparking or acoustically (crackling noise). For example,

Table 1 Parameters of oxide growth on valve metals

Metal / Alloy	Oxide				Ref.
	E_g (eV)	N (cm ⁻³)	ϵ_{ox}	type	
Al	4.5-9	-	7-20	i	69
Al/Cr	-	-	-	n	70
Cr	2.5-3.5	$\approx 10^{20}$	30 ± 20	p(n)?	71-76
Cu	0.6-1.8	?	7-18	p	69, 77
Fe	1.8-2.2	$\approx 10^{20}$	10-35	n	e.g., 78-80
Fe/Cr	1.9-2.1	10^{20} - 10^{21}	10-30	n	81
Fe/Cr/Ni (AISI304)	1.9-2.3	10^{20} - 10^{21}	10-30	n	82-85
Fe/Cr/Ni/Mo (SMO254, DIN1.4529)	2.3-2.8	$\approx 10^{21}$	10-30	n	84-86
Fe/Ni (xNi < 40%)	1.9	$\approx 10^{20}$	10-35	n	81
Ni	2.2-3.7	10^{20}	≈ 30	p(n)	71,80,87
Sn	3.5-3.7	10^{19} - 10^{20}	?	n	77
Ti	3.2-3.8	10^{20}	7-114	n	69
W	2.7-3.1	10^{17} - 10^{18}	23-57	n	77
Zn	3.2	$\approx 10^{18}$	8.5	n	77
Zr	4.6-8	-	12-31	i, n	69,77

E_g : band gap energy

N: doping concentration

ϵ_{ox} : dielectric constant

type: conduction type

n: n-type

p: p-type

i: insulator

Wood and Pearson [44] discuss anodic breakdown of oxide films on the valve metals Nb, Ta, Zr, Hf, Al, Ti, W, Mo, and V. It is of interest to note that according to these authors, Ti and W, whose oxide films are semiconductors, did not break down, but turned into conductors leading to oxygen evolution. Generally, breakdown on valve metals results in thickening of films at locations where the breakdown occurred, and thus pinches itself off. Wood and Pearson concluded that avalanche breakdown was being observed at sites where the electrons to initiate the avalanche are supplied by the electrolyte. At high voltages, the breakdown spot may meander over the surface, and for certain applications, extended anodization under these conditions ("spark anodization") is highly useful as it finally leads to a surface covered with an irregular structure of pores in the micrometer-size range – this has found interest to increase the biocompatibility of Ti-based biomedical implants [45, 46].

Under *cathodic* polarization, a range of valve metal oxides show significant cation in-diffusion, accompanying alterations in the electronic structure of the oxide (e.g., incorporation of additional states within the band gap). The most likely mobile species are protons. For example, Dyer and Leach [47] examined oxidized titanium and niobium and found that hydrogen enters the film under cathodic bias in non-negligible amounts. TiO₂, for example, can to a large extent (up to 85%) be converted to TiOOH, as concluded from observations of the change in the index of refraction. Thus cation in-diffusion into passivating films can be substantial under

cathodic bias. Hydrogen ingress into Ti oxide layers by cathodic polarization has recently also been studied by *in situ* neutron reflectometry [48].

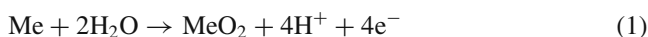
In general, current passage through oxide layers when the metals are biased cathodically is common on valve metals, for example, zirconium, tantalum, and aluminum, and oxides on silicon can show significant cathodic currents. Schmidt [49, 50] already suggested that these cathodic currents are related to the in-diffusion of protons, since with tantalum and silicon it was found that if an anhydrous electrolyte is used, there is no cathodic current. Vermilyea [51] and others [52] showed that the cathodic currents are laterally inhomogeneous and correspond to flaws in the oxide.

3 Formation of Nanotubular Layers

In the following, the formation of nanotubular (nanoporous) layers focuses on recent findings on their formation in fluoride-containing electrolytes, and will not address the classical case of Al – the interested reader may consider the chapter by Sides and Martin in this book for further references.

3.1 *I–U Curves*

A convenient way to characterize and compare the electrochemical behavior of valve metals are polarization curves (such as shown in Fig. 2). The electrochemical behavior of most valve metals in typical electrolytes, that is, electrolytes that do not chemically attack the oxide surface, is dominated by spontaneous oxide formation and growth. For example, in H_2SO_4 , electrolytes on the valve metals investigated in Fig. 2a, a compact layer forms according to reaction (1) with an increasing thickness the higher the voltage.



However, a clear deviation from the typical valve metal anodization electrochemistry is obtained in fluoride electrolytes [11, 53, 54] as shown in Fig. 2b. This is due to the fact that the oxide formed by reaction (1) is now chemically attacked (dissolved) by the formation of soluble fluoride complexes, for example:



If we compare the polarization curves shown in Fig. 2a and b, it becomes clear that the addition of a certain amount of fluorides shows, for the different valve metals, a different effect on the resulting current density. Clearly, on Zr and Hf, the highest steady-state current densities result, thus indicating a rapid dissolution rate of the oxides formed on the metal in HF. For Ti and W, these rates are lower, and for Nb and Ta, these rates are further reduced. This explains that for establishing

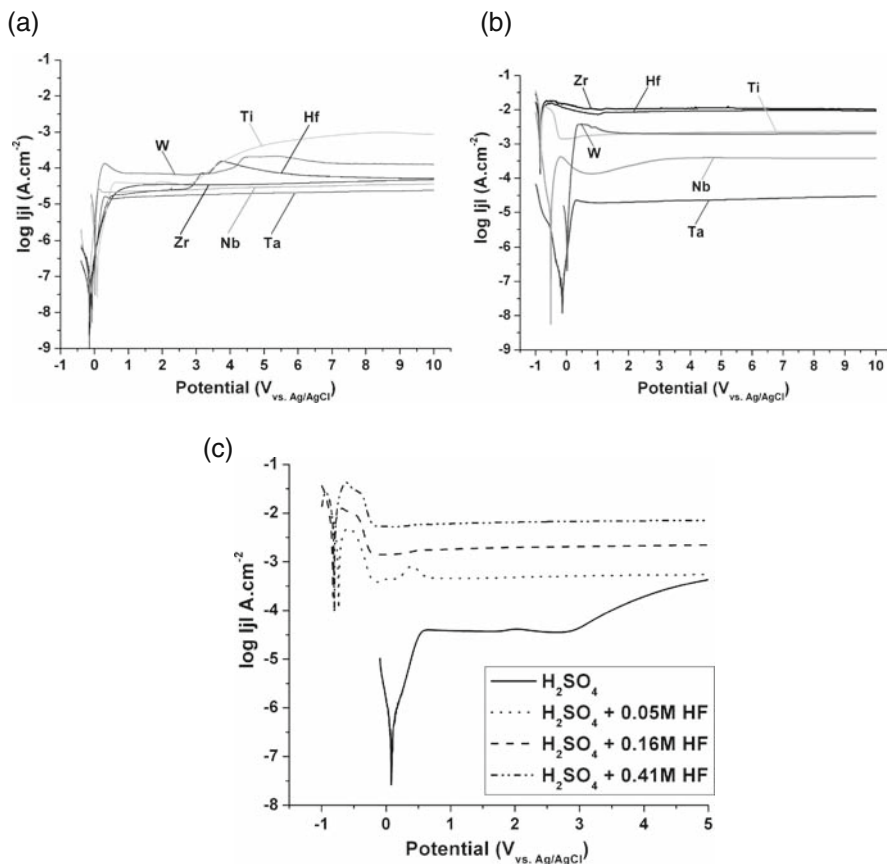


Fig. 2 Polarization curves recorded for valve metals in 1 M H₂SO₄ electrolyte without (a) and with 0.5 wt% HF (b), and (c) for Ti in 1 M H₂SO₄ with different HF concentrations

an electrochemical situation leading to pore formation, the fluoride concentration needs to be optimized for each valve metal.

This is shown for Ti in Fig. 2c. The addition of small amounts of F leads to activation of the surface – the polarization curves show an active/passive transition. The higher the fluoride concentration, the higher is the current density.

Scanning electron microscopy (SEM) observations of the surfaces after acquiring the polarization curves typically lead to the findings that anodization in solutions with a low HF concentration, for Ti typically <0.05 wt% HF, yields a compact oxide layer with a few nonregular pores. On the other hand, anodization in solutions containing >0.5 wt% HF leads to uniform etching of the surface (electropolishing). Therefore, the most promising range to achieve the formation of porous oxide networks is the concentration range between 0.05 and 0.5 wt%.

3.2 *I-t* Curves and Initiation of Porous Layers

A common observation in porosification experiments is that establishing the final state of the self-organized structure formation requires an induction time. This is also apparent in electrochemical experiments.

Figure 3a shows a schematic current–time transient for anodization of Ti at the “right” voltage in an electrolyte, for example, H_2SO_4 in absence and in presence of the “right” amount of fluoride. In pure background electrolyte (H_2SO_4), the typical exponential current decay is observed due to the growth of a compact oxide layer. For electrolytes containing fluorides, after an initial exponential decay (phase I) the current increases again (phase II) with a time lag that is shorter, the higher the fluoride concentration. Then, the current reaches quasi-steady state (phase III). This steady-state current increases with increasing fluoride concentration.

This type of current–time curves have been previously reported for self-organized pore formation for other materials, as well [55]. Typically, such a current behavior

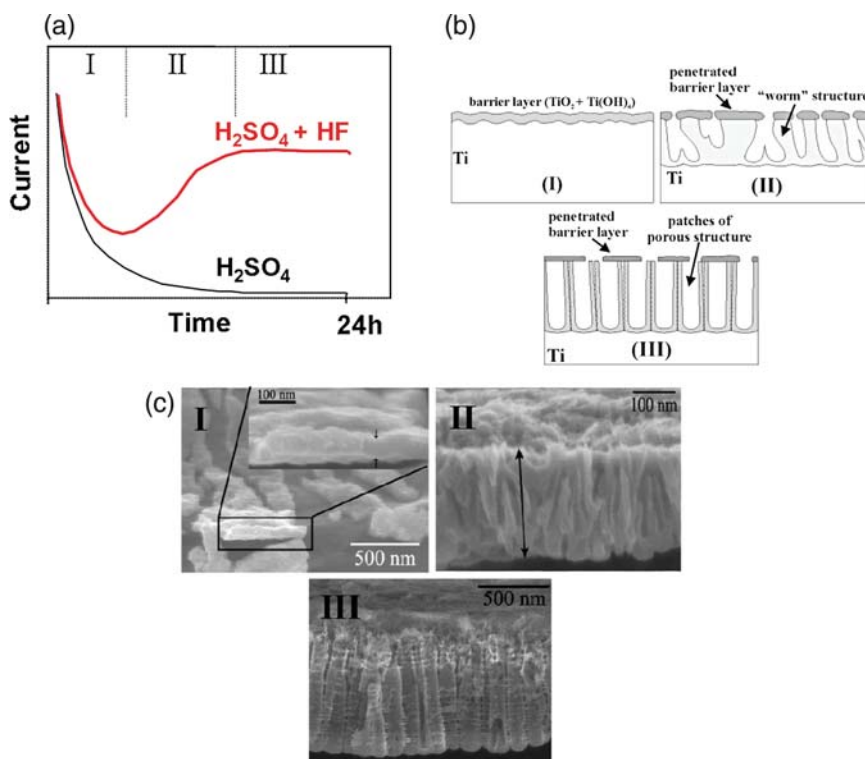


Fig. 3 (a) Schematic current transient for anodization of Ti in H_2SO_4 electrolyte without (a) and with HF; (b) scheme of pore formation process, (c) SEM images of corresponding stages in (b). Samples anodized in 1 M $(\text{NH}_4)_2\text{SO}_4 + 0.5$ wt% NH_4F at 20 V for 0 min (I), 6 min (II), and 20 min (III)

can be ascribed to different stages in the pore-formation process, as schematically illustrated in Fig. 3b. In the first stage, a barrier oxide is formed, leading to a current decay (I). In the next stage, the surface is locally activated and pores start to grow randomly (II). Due to pore growth, the active area increases and the current also increases. After some time, many pores are initiated and a tree-like growth takes place. Therefore, the individual pores start interfering with each other and start competing for the available current. This leads under optimized conditions to a situation where the pores equally share the available current, and self-ordering under steady-state conditions is established (III).

Indeed, if the pore initiation phase is followed in a concrete case by SEM images, the exact sequence described in Fig. 3b can be observed. Figure 3c shows samples removed from the electrolyte at different times – shown here is the evolution of the morphology of the porous titanium oxide in 1 M $(\text{NH}_4)_2\text{SO}_4$ + 0.5 wt% NH_4F [14]. Immediately after the sweep from the OCP to 20 V, a thin and rough layer (≈ 50 nm) covers the entire surface of the titanium (I). The results from XPS measurements show that the film at this stage is composed of Ti, O, and some traces of F. The XPS data suggest that the film is composed of an inner layer of TiO_2 and an outer layer of $\text{Ti}(\text{OH})_4$. This layer is essentially the fluoride-perforated high-field passive layer – the thickness very well corresponds to a growth factor of 2.5 nm V^{-1} . After some polarization time, the first signs of localized attack become apparent with the FE-SEM; breakdown sites that are randomly distributed over the film surface and round-shaped holes in the substrate can be observed. Then the current increases due to the growth of the pores. At this point, the SEM image reveals that underneath the initial 50-nm-thick top layer some pore structures become visible. This means that the top layer, in fact, must be of a nanoporous nature (beyond the resolution of SEM), permeable to fluorides and electrolyte species. In the cross-section, the mesoporous layer underneath the nanoporous layer shows a thickness of 200–300 nm and a relatively regular but worm-like structure (II). At this time, from the top, patches of the top layer are still visible but they dissolve with time in the F-containing electrolyte. With increasing anodization time, the current drops further, while a steady state of the porous film thickness establishes (III), and a homogeneous self-organized porous structure is obtained.

3.2.1 Current Oscillations

Inspecting in detail the I-t behavior in fluoride-containing electrolytes shows that periodical current fluctuations occur [11, 16]. The oscillations can be very regular and can be maintained for more than 24 h. Typically, the average amplitude and frequency increase with increasing HF concentration. The origin of these oscillations is not understood in detail. However, for other systems such as porous silicon formation, under specific conditions, strong current oscillations have also been reported [56]. A most likely explanation is that these current oscillations can be ascribed to passivation and depassivation reactions on the surface that are competing. Interestingly in the present case, the periodicity of the oscillations can be correlated with some structural features observed in the porous layer. Figure 1a shows an SEM

image of a TiO_2 nanotube layer with regularly spaced ripples at the side walls of the tubes. These ripples have a distance of about 50 nm. On the other hand, for the corresponding current oscillations, a frequency of 1/50 s can be determined with a current density of 3 mA/cm^2 , corresponding to approximately 1 nm/s dissolution rate. Hence, one period per 50 s corresponds very well to the observed length scale of the ripples in the side walls. Nevertheless, the exact description of the interactions between the current oscillations and structural features remains till date unresolved.

3.3 Steady-State Growth

The features of the tubes shown in Fig. 1a (thickness and side-wall morphology) are typical for nanotube layers grown in acidic electrolytes. In acidic electrolytes, the tubes grow with time only up to a limiting thickness of approximately 500–800 nm. A typical thickness versus time behavior is shown in Fig. 4a.

The fact that the layer thickness (Fig. 4a) and the current density (Fig. 3a) reach a limiting value after a certain polarization time can be explained by a steady-state situation depicted in Fig. 4b. During anodization, permanent growth of oxide takes place at the inner interface, and chemical dissolution of the oxide layer occurs simultaneously. Steady state is established when the pore growth rate at the inner interface is identical to the overall dissolution rate of the oxide film at the outer interface. In this situation, the nanotube oxide layer just permanently “eats” through the titanium substrate without thickening of the oxide layer. As the steady-state current densities are typically considerably high, this occurs even with comparably high velocity. This finding also explains that typical current efficiencies (for oxide formation) in acidic electrolytes range from 3% to 10%, and continuously drop with extended anodization time.

It should be remarked that the picture shown in Fig. 4b is somewhat oversimplified. The chemical dissolution of TiO_2 occurs, of course, over the entire tube length, thus the tubes with extended time become increasingly V shaped in morphology as shown in Fig. 4c. That is, at the top the tubes possess a significantly thinner wall than at their bottom [57, 58].

Several experiments and calculations show that these tubes grow under diffusion control conditions with either the supply of fluoride ions to the tube tip or the transport of the MF_6^{2-} complex away from the tube tip being the rate-determining step.

4 Factors Affecting Tube Morphology

4.1 pH of the Electrolyte

The limiting porous oxide layer thickness can to a large extent be overcome by altering the electrochemical conditions [12–14, 59]. This means, most importantly, that a higher thickness of the porous layer can be obtained if the anodization

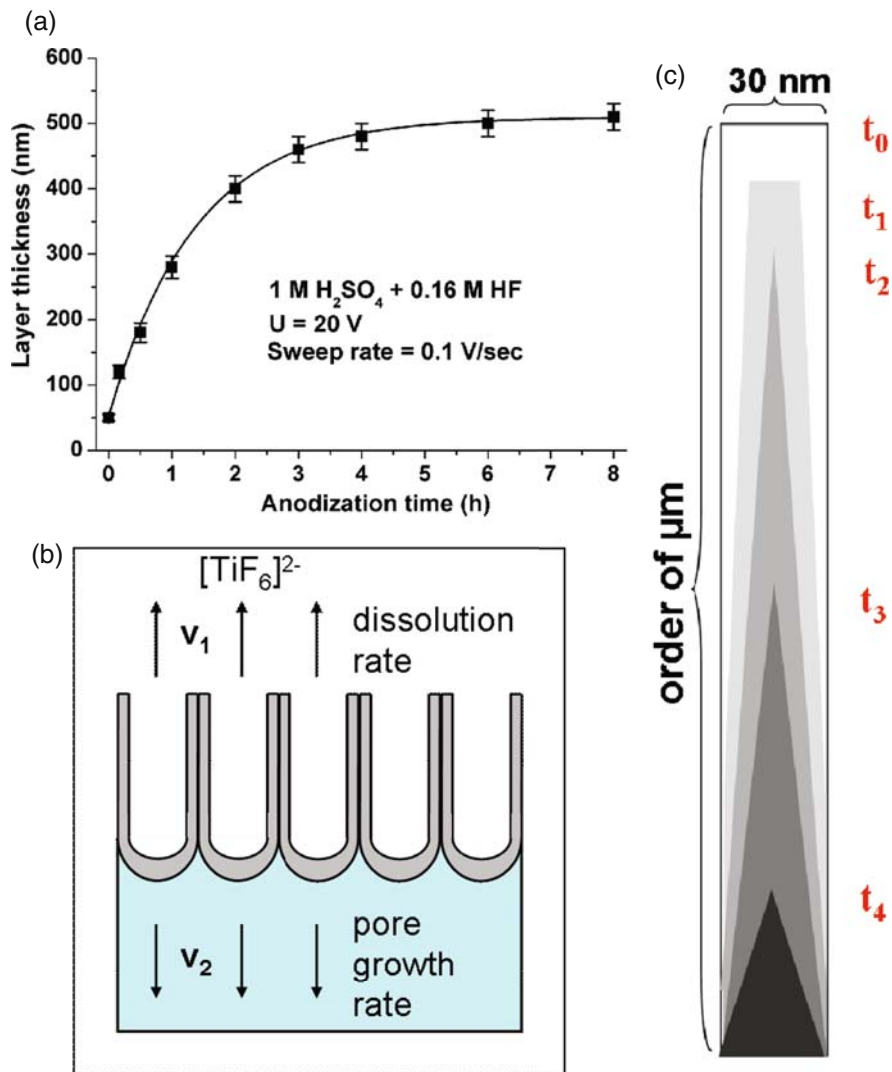


Fig. 4 (a) Evolution of tube layer thickness during anodization; (b) steady-state competition of TiO₂ dissolution and formation during the pore growth; (c) typical V-shape of the tube wall

treatment is carried out in less aggressive (more alkaline) electrolytes. Figure 5a shows the chemical dissolution rate of TiO₂ in fluoride-containing electrolyte as a function of the solution pH. Clearly, the more alkaline the solution, the lower is the dissolution rate, and therefore one could slow down the chemical dissolution of the oxide. However, to maintain pore growth at the pore tip, a certain degree of acidity (dissolution) is needed. The key to longer tubes is to recognize that this acidity can be automatically provided by the water hydrolysis reaction in the

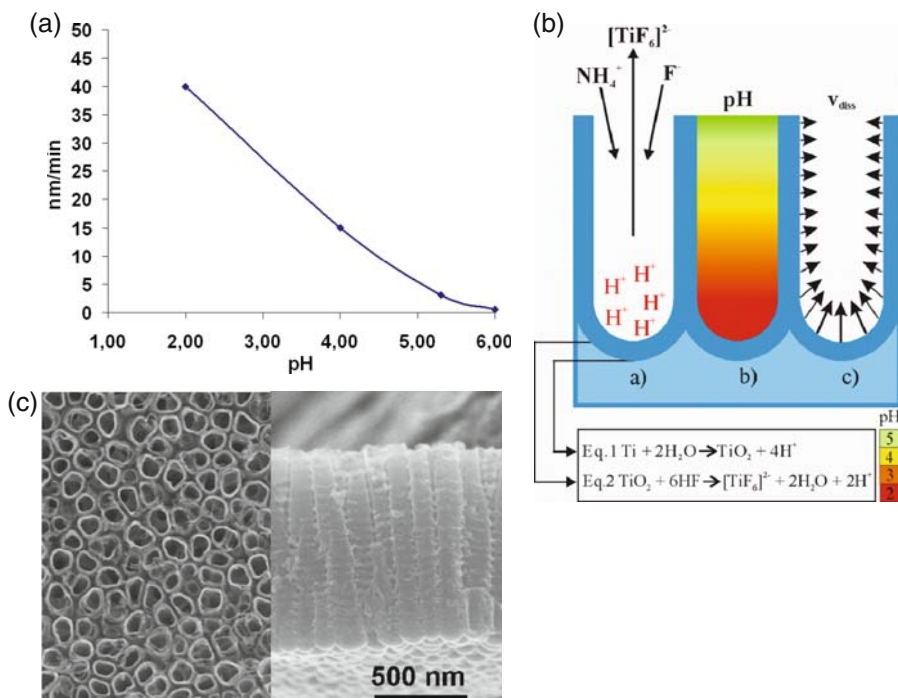


Fig. 5 (a) Dissolution rate of TiO₂ measured by XPS depth profiles on flat anodic TiO₂ samples of defined thickness after soaking in F-containing electrolytes with different pH; (b) pH profile inside the tubes; (c) example of a thick TiO₂ nanotube layer (SEM, top view, and cross-section)

oxide formation as shown in Fig. 5b. If the anodization is carried out in a neutral electrolyte, this acidification accelerates the chemical TiO₂ dissolution exactly at the desired place: at the pore tip (while the rest of the porous structure remains relatively stable due to the more alkaline pH of the background electrolyte) – for more details see Ref. [13]. Figure 5c shows top view and cross-sectional SEM image of an example of a thick TiO₂ nanotube layer produced in a neutral electrolyte.

4.2 Effect of Anodization Voltage

The key factor controlling the tube diameter is the anodization voltage [60]. Experiments carried out in 1 M H₃PO₄ + 0.3 wt% HF – see Fig. 6 – showed that in a potential range between 1 and 25 V, tubes could be grown with diameters from 15 to 120 nm and length from 20 nm to 1 μm, where diameter and length depend linearly on the voltage. Up to potentials of 25 V, self-organized tubular layers are obtained.

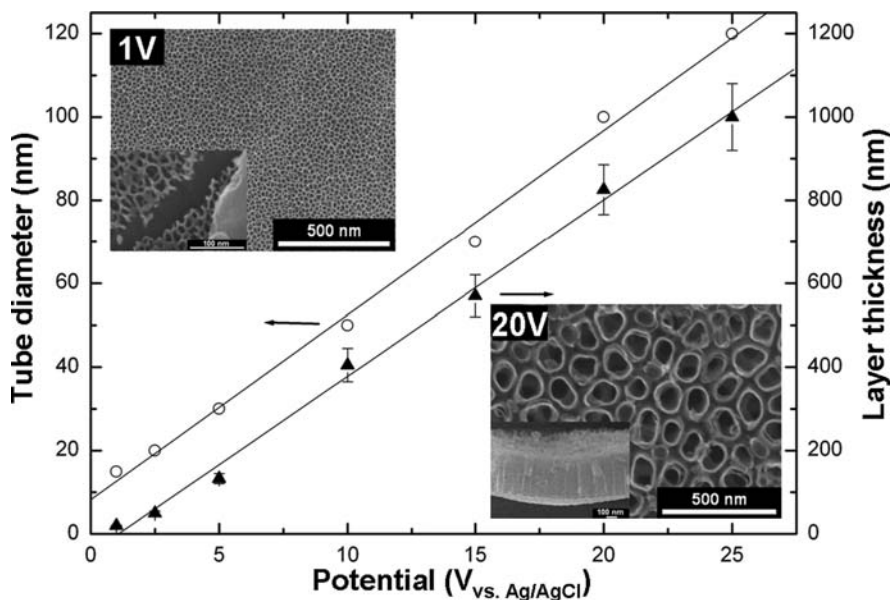


Fig. 6 Tube diameters and length as a function of anodization potential. Electrolyte 1 M H_3PO_4 + 0.3 wt% HF. Insets show SEM images of the nanotube layers formed at 1 and 20 V

At potentials higher than 25 V, the formed layers were no longer self-organized. Particularly remarkable is that self-organized structures are obtained even at potentials as low as 1 V. This may be a specific feature of the H_3PO_4 base electrolyte, as other electrolyte systems used for the formation of TiO_2 nanotubes typically show nonordered etched surfaces at such low voltages. Potentials lower than 1 V cause more or less uniform etching of titanium due to the fact that they reach the active corrosion region of the system.

The morphology features formed at 1 V show rather a web-like structure than a clear tubular morphology. Tubes formed at lower voltages are more connected to each other, whereas the nanotubes formed at 25 V seem to be more isolated from the surrounding ones.

This level of diameter control bears significant potential for applications where the tube diameter needs to be tailored for specific use, such as, for example, when a defined size for embedding of biological species is desired.

4.3 Effect of Viscosity

A series of experiments performed in ethylene glycol and glycerol water mixtures [16, 61] demonstrate clearly a strong influence of the electrolyte viscosity on the tube geometry. The tubes formed in these electrolytes show typically a smooth appearance over their entire length and grow to a significantly higher length – an

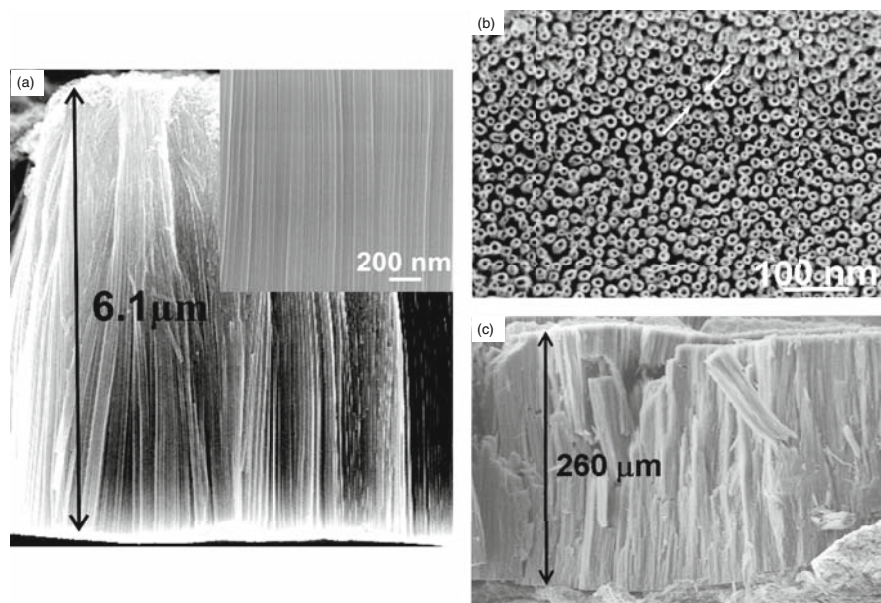


Fig. 7 SEM images of examples of TiO₂ nanotube layers grown in glycerol/NH₄F electrolyte (a) acetic acid/NH₄F electrolyte (b) and in ethylene glycole/HF electrolyte

example is shown in Fig. 7a. Evidently, the tubes are grouped in very tight bundles and are not connected with one another through any bulk material – this is in contrast to all previous growth attempts in literature, where a connection of the side walls (as in Fig. 1a) was always obtained.

In order to explain the smooth appearance, one may consider that current oscillations occur in aqueous electrolytes of low viscosity [11, 16]. The current transient frequency correlates well with the variations in the wall thickness. This can be explained by the fact that every current transient is accompanied with a pH-burst occurring at the pore tip. In viscous electrolytes, clearly the current–time transient shows much lower current densities than in the purely aqueous electrolyte – this is due to a lower diffusion constant in the electrolyte (considering the Stokes–Einstein relation where the diffusion constant, D , is proportional to $1/\eta$, where η is the solution viscosity). In other words, an increased diffusion constant keeps the acidic range more confined to the pore tip, thus it hampers dissolution of the tube walls and damps oscillations.

4.4 Effect of Water Content

In line with observations of other systems, anodization in (almost) water-free electrolytes can drastically increase the achieved length. Experiments carried out in CH₃COOH systems (example shown in Fig. 7b) showed a remarkable control over

the tube diameter [62]. Early work carried out in glycerol showed tubes with length in the range of 7 μm [16] – meanwhile the maximum length reached 260 μm as shown in Fig. 7c [63]. In this case, the tubes were grown in an aged ethylene glycol HF electrolyte with a rest H_2O content of 0.3%. Examination of the structure clearly shows that, at the bottom, a hexagonal cell structure prevails (as in the case of Al), and only the upper part is separated into tubes by chemical dissolution – as discussed in Section 4.1.

4.5 Formation of Multilayers and Free-Standing Membranes

Very recently it has been shown that for a range of valve metal oxides, multilayered structures can be grown [58, 64]. In other words, first, a layer under a first parameter set may lead to a first geometry, and then underneath, a second layer of tubes can be grown with a different parameter set. Interestingly, the underneath layer may be initiated at the bottom of a tube to break through the bottom [64], or in the spaces between the tubes [58]. Such multilayer stacks may have a variety of applications wherever critical tailoring of properties is needed.

Even more spectacular is the formation of free-standing (open porosity) membranes [65] as a whole range of functionalization may be accessed, including, for example, flow-through photoreactors.

4.6 Different Metal Substrates

Except for Ti, on a range of other valve metals, some self-organized structures have been grown and significantly different morphologies obtained.

Zr, Hf:

In comparison with other valve metals, the most straight-forward formation of nanoporous or nanotubular layers can be achieved on Zr and Hf [18, 19, 26]. On the materials, without a lot of experimental optimization, long and smooth tube morphologies can be easily grown. In contrast to other anodic valve metal nanotubes, the oxide tubes grown on Zr and Hf have a crystalline structure directly after anodization (i.e., without annealing). Zirconium oxides are known to have excellent technological properties, such as chemical and thermal stability, mechanical strength and wear resistance, as well as its good ion-exchange properties. These properties enable zirconium oxide films to be used as industrial catalyst and catalyst supports for its particular acid catalysis. A great effort has been made to prepare porous zirconium oxide with a high surface area to improve the efficiency as a material in catalysis. Therefore, some research efforts have focused on the synthesis of porous zirconium oxide by using templating techniques [66–68] and electrodeposition [67, 69]. Compared with aluminum and titanium, however, only a few early studies report on random patches of porous zirconium oxide structures formed during anodization [70, 71]. The use of fluoride containing acidic electrolytes lead to porous material rather

than tubular structures; however, smooth high-aspect-ratio zirconia nanotubes were fabricated by electrochemical anodization of zirconium in neutral buffers [18, 19].

These high-quality zirconia nanotube layers consist of highly regular arrays of straight nanotubes with a diameter of 50 nm and a length of 17 μm , with pore walls that are completely smooth and straight. The grown nanotubes were found by XRD and TEM-SAED to have a cubic crystalline structure without any further heat treatment.

Similar findings were obtained for HfO_2 in H_2SO_4 electrolytes containing NaF [26]. Under a range of experimental conditions, highly ordered tube-like structures can be formed. The pore diameter increases with increasing potential from ~ 15 to 90 nm. The porous oxide layers can be grown to a thickness of several-tens micrometer in a voltage range from 10 to 60 V.

Ta, Nb:

As already discussed in the section on I–U curves, it is more difficult to grow ordered nanotubular layers on Ta and Nb. Typically, only layers of some 100-nm thickness are obtained. Porous oxide structures on Nb bear high application potential as gas sensors [72], catalysts [73], optical [74], and electrochromic [75] devices. First investigations [21] reported porous Nb_2O_5 layers that consist of ordered-pore arrays with single-pore diameters ranging from 20 to 30 nm. The layers were formed in $\text{H}_2\text{SO}_4/\text{HF}$ electrolytes, and it was found that the pore morphology and the layer thickness strongly depend on the HF concentration and the time of anodization. Well-ordered uniform porous layers of up to 500 nm in thickness were formed using 1–2 wt% HF. Later work by Choi et al. [76] has shown the possibility of growing porous Nb_2O_5 layers also in $\text{H}_3\text{PO}_4/\text{HF}$ mixtures. Furthermore, they have increased their thicknesses by repeated porosification, that is, Nb_2O_5 layers were grown and annealed, and then a second anodization was used to form a second layer [77]. In recent work, additionally, Karlinsey has demonstrated that by anodization of Nb in HF electrolytes (0.25–2.5 wt% HF) Nb_2O_5 microcones can be grown on Nb surfaces [78].

Ta_2O_5 has received considerable attention as a protective coating material for chemical equipment, as part of optical devices, and as suitable material for storage capacitors in very large-scale integrated circuits [79–84].

Similar to Nb, on Ta the formation of porous Ta_2O_5 on Ta was investigated in H_2SO_4 electrolytes containing different concentrations of HF (0.1–5 wt%) [24, 25]. Porous (nanotubular) tantalum oxide that consists of pore arrays with single-pore diameters of about 20 nm and pore spacing of about 15 nm was obtained up to thicknesses of several 100 nm for HF concentrations of around 2% and several hours of anodization.

W:

Experimentally, the formation of porous (nanotubular) WO_3 is most challenging, but it is also most highly rewarding as tungsten is one of the most important valve metals, and its oxide has electrical and optical properties that are exploited for a variety of applications such as photolysis [85], electrochromic devices [86–88],

and gas sensors [89–92]. Several preparation techniques have been reported for the fabrication of tungsten oxides, for example, thermal evaporation [90, 91], chemical vapor deposition [92], and sol–gel coating [86–88]. Though anodization of tungsten in electrolytes is one of the methods to fabricate tungsten oxide and has been intensively studied, the formed films typically show a compact structure [93, 94]. In fluoride electrolytes (e.g., 0.2 wt% NaF) at elevated potentials such as 40 V and 60 V, well-structured porous arrays can be grown with 59–70 nm tube diameter and a thickness of several 100 nm [22]. As-formed layers show an amorphous structure, but the layers can be altered to a crystalline monoclinic structure by thermal annealing at 500°C. The annealed porous WO₃ layers show a very high specific photocurrent-conversion efficiency, reaching 20–30% in the UV range [95].

Alloys:

Attempts have been made to grow self-organized anodic tube layers on technologically relevant substrates such as Ti6Al4V and Ti6Al7Nb [9, 96, 97]. However, these approaches suffered typically from two problems: (1) the selective dissolution of less stable elements and (2) the different reaction rates on different phases of an alloy. In designing an “ideal” alloy for nanotube formation, one desires a single-phase microstructure and a composition that only contains elements that show similar electrochemical oxidation rates. Therefore, an alloy such as the recently developed TiNb, TiZr, or biomedical alloys such as Ti₂₉Nb₁₃Ta_{4.6}Zr [98, 99] have promising composition as they can be tuned to be a single phase (β -phase), and they consist only of elements on which nanotubes have successfully been grown in fluoride-containing media.

For TiNb, surprising synergistic effects on the growth morphologies of the oxide nanotubes were found [100]. It was shown that the range of achievable diameters and lengths of TiO₂-based nanotubes can be significantly expanded, if a binary Ti–Nb alloy, rather than pure Ti, is used as a substrate for oxide nanotube growth in an aqueous electrolyte. The length of the resulting mixed oxide nanotubes can be adjusted from 0.5 to 8 μ m, and the diameter from 30 to 120 nm. The morphology of the tubes differs significantly from that of the nanostructures grown under the same conditions on pure Ti or Nb substrates: only considerably shorter tubes grow on Ti, whereas irregular porous structures grow on Nb.

The tubes consist of an amorphous mixed TiO₂–Nb₂O₅ oxide structure. After annealing at 450°C, anatase-type TiO₂ appears in XRD. After annealing at 650°C, an additional peak assigned to rutile appears, but the major TiO₂ phase remains anatase with a crystallite size of 25 nm. This result shows that the anatase–rutile transition takes place at a higher temperature in the polycrystalline mixed-oxide nanotubes than in pure TiO₂.

Weak reflections assigned to pseudo-hexagonal TT–Nb₂O₅ can be detected after annealing at 650°C. Apart from the retardation of the anatase–rutile transition by Nb₂O₅, it is also remarkable that the mixed-oxide nanotubes are stable to annealing at 650°C. For pure TiO₂ nanotubes treated at this temperature, a substantial collapse of the tubular morphology has been reported [101]. Very recently, high-efficient intercalation properties have been reported for this alloy [102].

For anodic nanotubes formed on TiZr alloys [57, 64, 103], the morphological character of the oxide nanotubes is between those of titanium oxide and zirconium oxide nanotubes. However, the nanotubes have a straight and smooth morphology with a diameter ranging from 15 to 470 nm and a length up to 21 μm depending on the terminal anodization potential (i.e., they show a largely expanded structural flexibility compared with nanotubes formed on the individual elements). In contrast to nanotubes formed on TiNb, the tubes grown on TiZr consist of a zirconium titanate oxide – as formed, with an amorphous structure that can be crystallized after adequate heat treatment [103].

Such nanotube structures are interesting in view of several applications, as zirconium titanate (ZT) is used as microwave-resonant components and frequency-stable oscillators [104–106], optical devices [107, 108], refractory ceramics [109], and template for lead zirconium titanate (PZT).

The alloy Ti₂₉Nb₁₃Ta_{4.6}Zr has been developed by Niinomi et al. for biomedical applications in order to reduce the elastic modulus of titanium alloys to the level of living bone [110]. Self-organized oxide nanotubes grown on this alloy [98, 99], except for a high degree of structural flexibility, can show a very spectacular feature, that is, multiscale self-organization (oxide nanotube arrays with two discrete sizes and geometries).

Additionally, one may note that recently it was demonstrated that also for the Al case, neutral F-containing solutions can be used to achieve fast and highly ordered oxide structures [111].

5 Structure and Chemistry

5.1 Crystallographic Structure

As-formed TiO₂ tubes typically have an amorphous structure. However, different TiO₂ applications require specific crystallographic structures for an optimized performance. For example, the anatase form of TiO₂ shows the highest solar energy conversion efficiency [112] and has also the highest activity for catalysis [113]. Several studies show that the tubes can be converted to anatase or a mixture of anatase and rutile at temperatures higher than approximately 280°C in air [101, 114, 115].

Figure 8a shows a comparison of XRD patterns of nanotube samples after formation (amorphous), after annealing at 450°C (anatase), and after annealing at 550°C (mixture of anatase and rutile).

Figure 8b shows high-resolution transmission electron microscope (HRTEM) images of the bottom of the nanotubes before and after annealing and selected area diffraction patterns (SAED) of the tube bottoms taken from the corresponding images (as insets).

Figure 8b confirms the XRD measurements that upon thermal annealing the samples, a transformation from amorphous to crystalline structure occurs. From XRD measurements, one can obtain that the major anatase is the (101) plane. Other

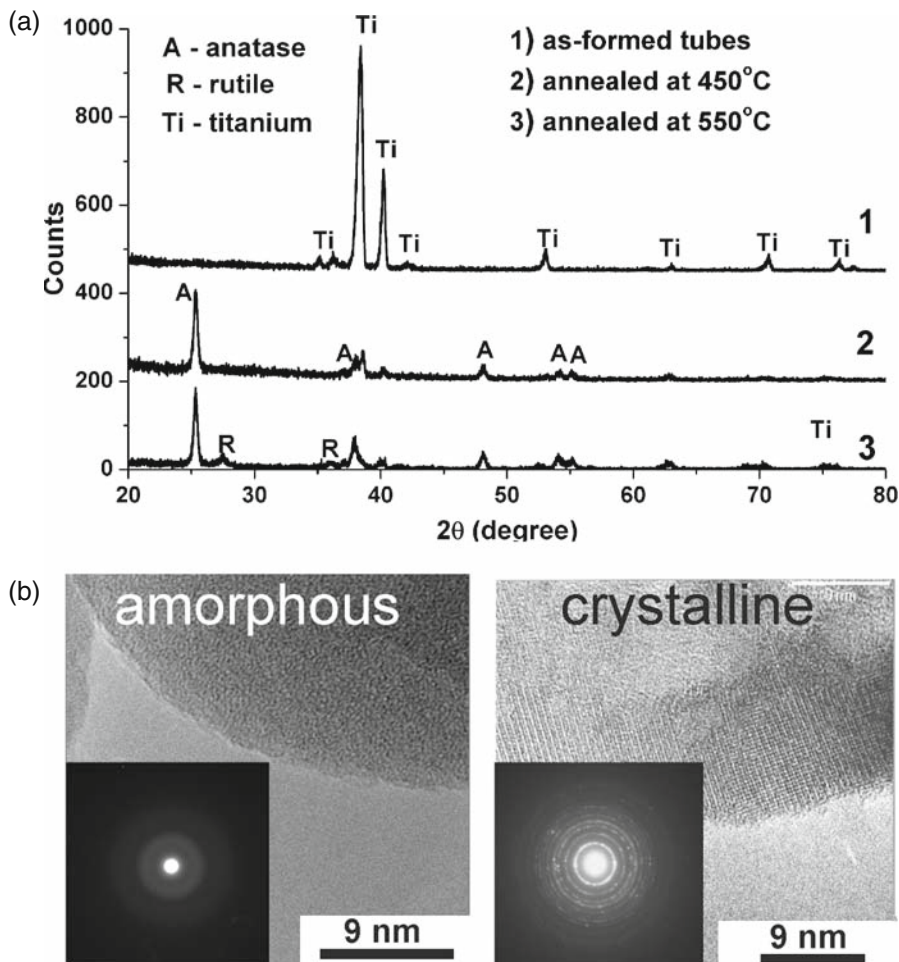


Fig. 8 (a) XRD of as-formed amorphous TiO_2 nanotube layer and crystalline layers annealed at 450°C and 550°C; (b) HRTEM images of amorphous(as-formed) and crystalline (annealed at 450°C) tube bottoms, insets shows diffraction patterns (SAED) taken at the same locations. Annealing performed for 3 h with heating and cooling rate of 30°C min^{-1}

planes, such as (200) and (105) are only present in a minor amount. For the nanotube layers, typically, crystal growth starts at the tube bottom via interface nucleation, due to the larger space available for crystal growth, than in the side wall [101]. For certain tubes, it was found that essentially over the entire length, only one plane – (101) – is present along the walls. This points to the possibility of growing single crystalline tubes [115, 116].

Annealing under oxygen-free conditions (e.g., in argon atmosphere) leads to a blackening of the tube layers due to a significant reduction of the Ti(IV) -species

in the oxide to Ti(III). Such structures typically have a very limited mechanical stability [114].

Annealing in air at temperatures above 450°C typically leads to increasing rutile content. At temperatures around 650°C and higher, the tube layers start losing their morphological integrity – that is, they start collapsing [101, 114].

Introducing alloying elements such as Nb [117] or C [118] into the TiO₂ increases significantly the temperature of the anatase-to-rutile conversion and also shifts the temperature of structural collapse to a higher value.

5.2 Chemical Composition

In XPS and EDX investigations, as-formed tubes show a composition of TiO₂ with minor contents of hydroxides on the surface of the tube walls [14]. Different background ions in the electrolyte are integrated into the tube structure at different concentration levels. While ClO₄⁻ ions are hardly incorporated, SO₄²⁻ and particularly PO₄³⁻ are incorporated into the entire tube to significant levels (some few at.%). It is very clear that significant amounts of F⁻ (≈1–5 at.%) are entering the TiO₂ structure. This is in line with some earlier work on the anodization of Ti in fluoride containing electrolytes [119]. An example of a XPS sputter depth profile is shown for nanotube TiO₂ layer in Fig. 9.

Annealing leads to almost a complete loss of the fluorides at around 300°C [116] and clearly the amount of surface hydroxides is reduced [120, 121].

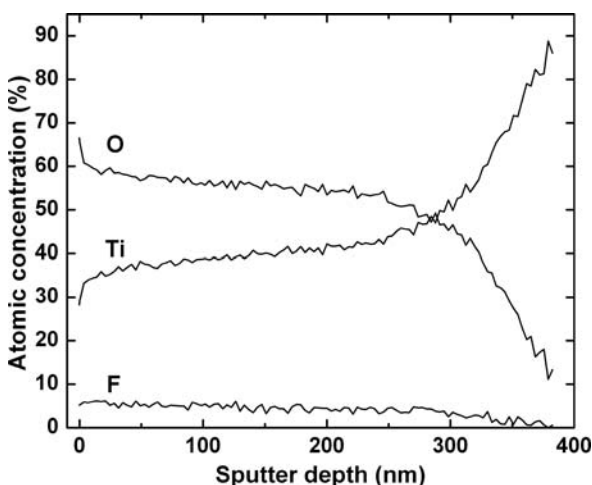


Fig. 9 XPS depth profile of nanotubular TiO₂ layer formed in 1 M H₂SO₄ + 0.16 M HF at 20 V. Thickness is approximately 350 nm, fluoride uptake is visible

6 Properties of the Tubes

6.1 Photoresponse of the Tubes

Typical photocurrent characteristics for the as-formed and annealed samples are provided in Fig. 10 [114, 122]. The comparison shows IPCE plots for the annealed nanotubular TiO_2 and the annealed compact TiO_2 . The inset figure gives the corresponding $(IPCE h\nu)^{1/2}$ versus $h\nu$ plots for these samples. Clearly, the band gap results also for the annealed samples as 3.15 ± 0.05 eV which is in line with typical value reported for anatase [123, 124]. It is evident that the IPCE is drastically increased for the tubes – that is, for the annealed tubes a value of almost 50% at short wavelength (compared to 10% for the annealed compact layer and 3–4% for the unannealed tubular or compact samples). In fact, for the as-formed tubes, most of the photocurrent is generated at the bottom of the tubes, and the tube wall contribution is negligible. This is in line with the expectation that the amorphous structure provides a high number of defects that lead to a high carrier recombination rate. The drastic increase of the photocurrent after annealing indicates that by conversion to anatase the tube walls are activated and contribute to the photocurrent. The voltage dependence of the photocurrents recorded for annealed nanotubular and compact TiO_2 layers showed that an enhanced photocurrent is obtained essentially over the entire potential range. However, at potentials (E) close to the flat-band situation (the optical flat-band potential E_{fb} is approximately at -0.2 V_{Ag/AgCl} in neutral solutions), the absolute photocurrent response for the nanotubes can be up to 20 times higher

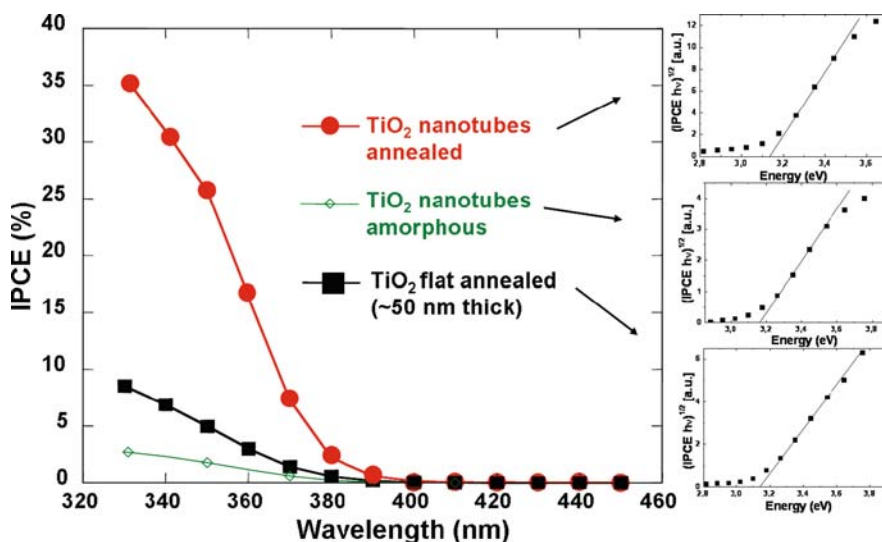


Fig. 10 Photocurrent spectra recorded for as-formed and annealed (as in Fig. 8) TiO_2 nanotube layers and for comparison also for compact anodic TiO_2 layer. Insets show evaluation of the band-gap energy (E_g) of the respective layers

than for the compact oxide. At higher anodic potentials ($E > 1$ V), a saturation of the photoresponse is observed. The potential dependence is very well in line with expectations of $i_{ph} \propto E^{0.5}$.

Further details of optimizing the tube geometry (length, diameter, and tube wall thickness), structure (anatase and anatase/rutile) need to be carried out. Presently, highest conversion efficiencies are achieved with tubes annealed to anatase and a length of approximately $300 \text{ nm}^{-1} \mu\text{m}$. This is due to a competition between most-efficient light-absorption length and increased recombination with increased length.

6.2 Doping, Dye Sensitization

In general, in order to enhance the efficiency of TiO_2 in the visible range, considerable efforts have been made involving dye sensitization [28, 112] of the electrode with suitable species, which showed that certain organic dyes (mainly Ru-complexes) fixed on TiO_2 can inject electrons into the conduction band of TiO_2 upon light excitation (as the LUMO overlays with the conduction band edge of TiO_2). As the HOMO/LUMO distance of these dyes typically is only 1–2 eV, the reaction can be triggered by visible light. The dye can be attached on TiO_2 surfaces by $-\text{COOH}$ coupling – the oxidized dye can be reduced by a suitable redox species to again form the active (reduced) state on the surface. Also with the nanotube layers, successful dye sensitization has been demonstrated using a commercial Ru-dye as shown in Fig. 11a [125].

A completely different approach is the so-called doping of TiO_2 (Fig. 11b). Asahi et al. [126] reported that doping TiO_2 with nitrogen by sputtering in a nitrogen-containing gas mixture improves the photoelectrochemical reactivity of TiO_2 films toward organic molecules under visible light illumination. Other doping species,

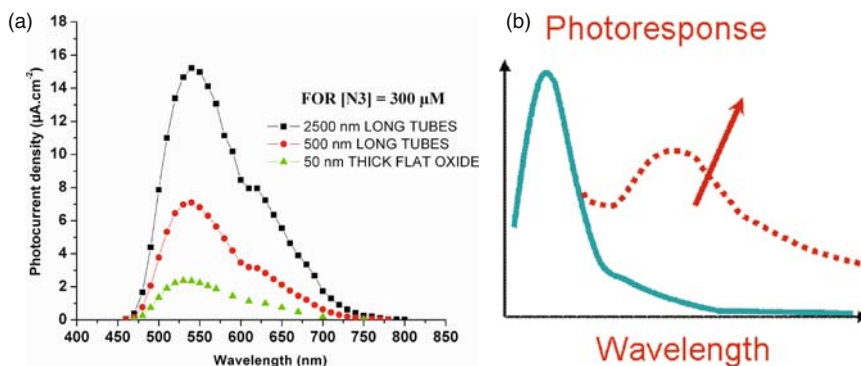


Fig. 11 (a) Photocurrent spectra of dye-sensitized samples (N3 dye) measured in acetonitrile + KI + I_2 electrolyte; (b) schematic picture of doping the TiO_2 toward visible light photoresponse

such as a number of transition metals [127, 128], or nonmetals such as phosphor [129], fluorine [130], carbon, [131], sulfur [132, 133], and boron, [134] have been introduced into TiO_2 compact layers or powders using various techniques. Ion implantation is the most straightforward approach for doping, but, up to now, efforts carried out on TiO_2 (by transition metal implantation) were hampered by the accompanying structural damage [128].

Considerable nitrogen doping of the tube layers was achieved by ion implantation [135, 136] and by thermal treatment in NH_3 [137, 138], wet chemical approaches [139] show only limited success. Other elements such as Cr [140] or C [141, 142] have also led to structures with a considerable visible light response.

6.3 Insertion Properties for Li and H^+ and Strong Electrochromic Effects

Another specific property of TiO_2 is its ability to serve as a host for hydrogen ion or lithium ion insertion [143–146]. These insertion reactions take place under cathodic polarization and are accompanied by reduction of Ti^{4+} to Ti^{3+} and a change of the color of the material [147].

The kinetics and magnitude of ion insertion and the electrochromic reaction (contrast) strongly depend on the ion diffusion length and therefore on geometry of the electrode surface. Due to the specific geometry of the TiO_2 nanotubes, a very high contrast can be obtained using vertically oriented nanotubes [148].

For example, Fig. 12a shows the cyclic voltammograms in a 0.1 M HClO_4 electrolyte for a compact anodic TiO_2 layer and a TiO_2 nanotube layer. The cathodic

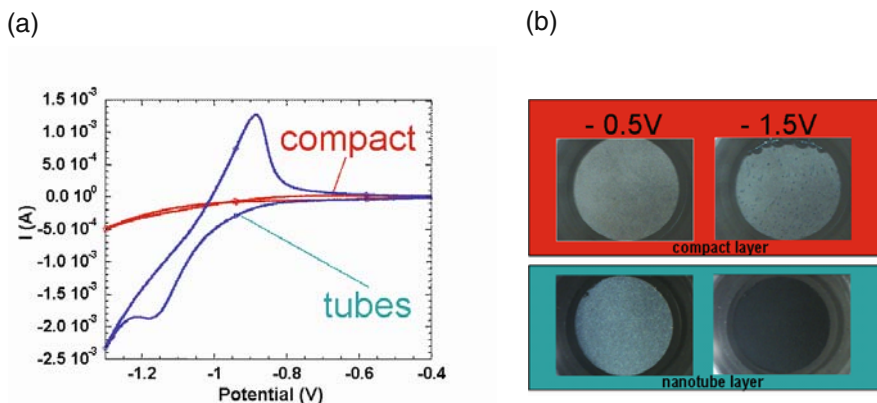
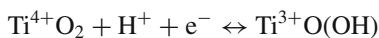


Fig. 12 (a) Cyclic voltammograms recorded for nanotube and flat TiO_2 layers in LiClO_4 and (b) corresponding optical images of the samples showing strong electrochromic switching effect observed at different potentials

peak can be ascribed to Ti^{4+} reduction combined with H^+ intercalation (Eq. (1)) while the anodic peak can be ascribed to the counter-reaction (i.e., the H^+ release reaction) [149]:



The reaction occurs relatively sluggish (and hardly at all) on the compact oxide layer and on the as-formed nanotubular TiO_2 structure, while it is more pronounced for the annealed (anatase) structure.

While scanning from anodic to cathodic values, a very clear modification of the color can be observed for the nanotube layer by the naked eye – in these cases, the color changed from a very light gray to a solid black. On the compact oxide surface, however, hardly any color change could be observed by eye. This is shown in Fig. 12b. Similar findings were observed for Li insertion reactions [150].

6.4 Photocatalysis

After Fujishima and Honda reported, for the first time, on light-induced water splitting on TiO_2 surfaces, the material has been intensively investigated for applications in heterogeneous catalysis [27]. Since then, TiO_2 has shown to be an excellent photocatalyst [113, 151, 152] with a long-term stability, low-cost preparation, and a strong-enough oxidizing power to be useful for the decomposition of unwanted organic compounds [153–155].

The principle of the photocatalytic decomposition is that photons from a light source, which have sufficient energy, that is, higher than the band-gap energy – E_g – of the TiO_2 , excite electrons from the valence band to the conduction band of the semiconductor and charge carrier pairs (consisting of hole h^+ and electron e^-) are formed [156]. These charge carriers either recombine inside the particle, or migrate to its surface, where they can react with adsorbed molecules. In aqueous solutions, positively charged valence band holes from TiO_2 typically form $\cdot\text{OH}$ radicals, while electrons in the conduction band mainly reduce dissolved molecular oxygen to superoxide $\cdot\text{O}_2^-$ radical anions. Organic molecules present in the solution may react with these oxidizing agents, inducing their oxidative degradation to inorganic compounds, including carbon dioxide and water [157]. In order to achieve a maximum decomposition efficiency, except for adequate band-edge positions, rapid charge separation, and high-quantum yield, a large area of the catalyst is desired.

Recently it has been demonstrated that the annealed TiO_2 nanotubes show considerably higher decomposition efficiency than a compacted Degussa P25 layer (20–30-nm diameter nanopowder composed of anatase and rutile) under comparable conditions [158], and even more recently, a flow-through membrane has been fabricated that is highly interesting for a large number of photocatalytic applications [65].

6.5 Highly Adjustable Wetting Properties

The ability to decompose organics on the surface combined with a nanotubular geometry can be used to tailor surface-wetting properties of TiO₂ from super hydrophilic to superhydrophobic [159, 160].

Titanium is a widely used biocompatible material; therefore, alterations of surface topography and wetting behavior are of great importance for its biomedical application. Several approaches using UV light [161, 162] or organic monolayers [163] have been reported to control the surface wettability of TiO₂ structures and nanoparticles.

The water-contact angle for freshly prepared flat TiO₂ samples is around $49 \pm 2^\circ$, while the nanotube structures showed a superhydrophilic behavior, that is, complete spreading of water on the entire surface and into the tubes. After the samples had been stored in the dark for 3 weeks, the water-contact angle for compact film increased up to $92 \pm 2^\circ$, whereas it remains unchanged for the tubular layers at $0 \pm 1^\circ$ – that is, the nanoporous layer still shows complete wettability (Fig. 13a). The change in wetting behavior of the compact TiO₂ with time has been ascribed to a change in surface termination [162] – that is, by ageing the hydrophilic OH groups convert into less hydrophilic oxide.

In order to alter the surface properties, octadecylsilane or octadecylphosphonic acid molecules can be attached to the TiO₂ surface [159, 160]. The originally completely hydrophilic surface becomes superhydrophobic, with a water-contact angle of about $165 \pm 2^\circ$ for the silane-SAMs and $167 \pm 2^\circ$ for phosphonic acid-SAMs (Fig. 13b). For comparison, the compact layers showed $107 \pm 2^\circ$ by organic modification.

Using UV illumination, the wetting behavior can be altered. After about 12 min for the silane-SAM and 5 min for the phosphonic acid-SAM (Fig. 13c), the porous surface changed from super hydrophobic (contact angle $\sim 165^\circ$) to complete hydrophilic behavior (contact angle $\sim 0^\circ$). Figure 13d shows the contact-angle change under UV illumination for different exposure times. This alteration can be stopped at any time leading to a very well-adjusted and stable surface with a well-defined wettability. XPS studies revealed, in line with literature [164], that during UV light treatment, organic monolayers start to decompose by chain scission at the functional end of the C chain leaving -Si-O⁻, -P-O⁻ groups behind (see Fig. 13e).

6.6 Biomedical Applications

Titanium and its alloys such as Ti-6Al-4 V and Ti-6Al-7Nb are widely used in biomedical applications for orthopedic or dental implants due to their good mechanical properties and biochemical compatibility [165]. Therefore, studies on the interaction of the nanotube material in regard to a biorelevant environment are of a very high significance. Mainly, two directions have so far been explored with TiO₂ nanotube coated substrates:

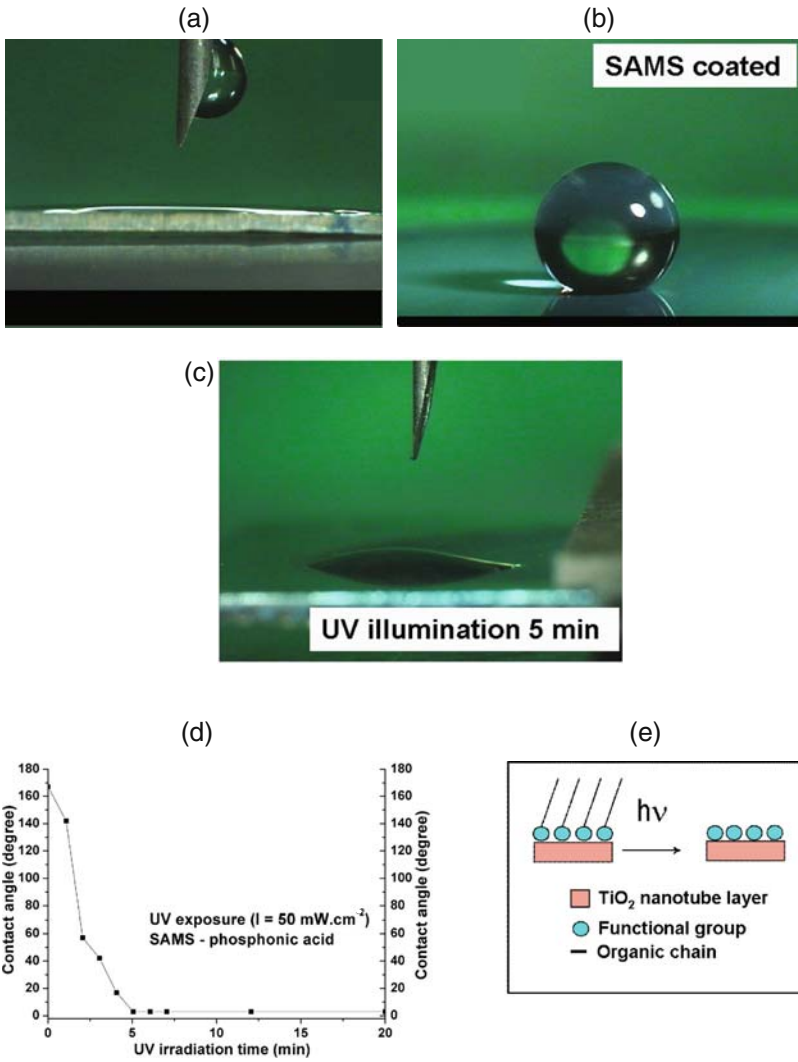


Fig. 13 Optical images of (a) superhydrophilic TiO₂ nanotube surface, (b) superhydrophobic surface coated with organic monolayer-phosphonic acid, (c) the same surface as in (b) after 5 min of exposure to UV light, (d) evaluation of the contact angle for sample in (b) upon exposure of UV light, (e) mechanism of photocatalytic decomposition of the organic monolayer on TiO₂

- (a) hydroxyapatite growth
- (b) cell interactions

(a) Hydroxyapatite growth

Apatite formation is considered to be essential for the bone-binding ability of biomaterials. In order to improve bioactivity of titanium and to enhance biocom-

patibility, surface treatments such as hydroxyapatite coating or chemical treatments have been exploited [166–173]. In particular, the chemical treatments in NaOH have been extensively examined [170, 171]. An electrochemical method to increase biocompatibility of titanium surfaces is spark anodization [45, 46, 172, 173], which typically leads to a formation of a rough random porous TiO₂ layers.

Recently, hydroxyapatite formation on TiO₂ nanotube layers with different tube lengths was investigated [174]. The nanotube layers could strongly enhance apatite formation compared with compact TiO₂ layers, as shown in Fig. 14. Surprisingly, the apatite coverage of the nanotube layers was dependent on the nanotube length – this was attributed to a different surface roughness of the different-length nanotubes influencing nucleation of hydroxyapatite precipitation. Annealing the nanotube layers (from amorphous structure) to anatase, or anatase and rutile, further enhanced apatite formation. The induction time for apatite formation on TiO₂ nanotube layers becomes comparable to the best other known treatments of Ti surfaces. It should be noted that also on alloys such as Ti6Al4V, Ti6Al7Nb, Ti29Nb13Ta4.6Zr (Niinomi alloy), formation of an ordered and robust oxide nanotube layer is possible [9, 96–99].

(b) Cell response to nanotube layers

Recently, studies were carried out using rat mesenchymal stem cells and primary human osteoblast-like cells that were seeded on TiO₂ nanotube structures,

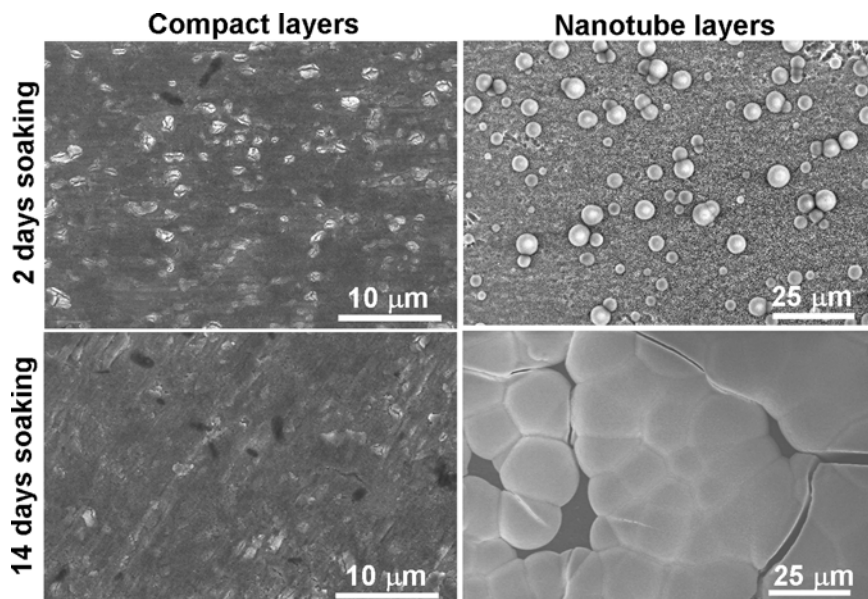


Fig. 14 SEM images of nanotube and anodic TiO₂ layers after 2 and 14 days of soaking in SBF solution

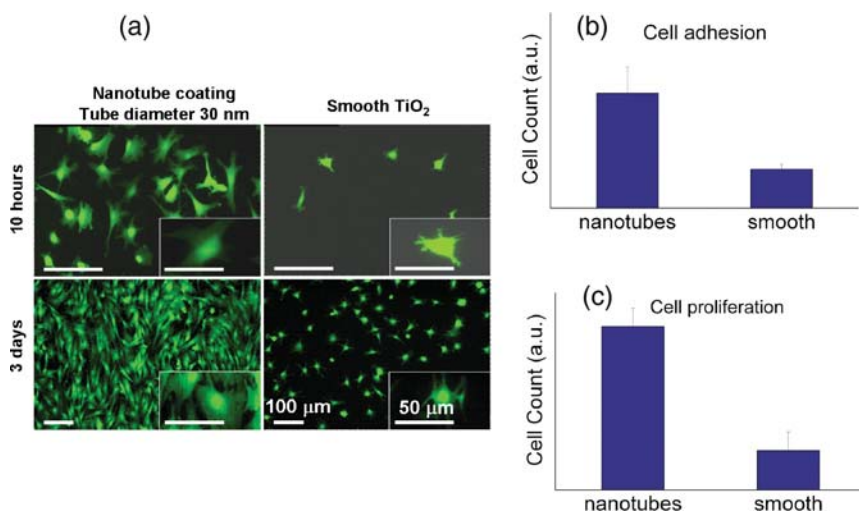


Fig. 15 (a) Cell behavior on nanotube TiO₂ layer (tube diameter ≈ 30 nm) compared with flat (smooth) TiO₂ layer. Tests done at 37°C with mesenchymal stem cell (GFP-labeled) using a cell density of 5000 cells cm⁻² and 5% CO₂; (b) cell adhesion after 24 h; (c) cell proliferation after 3 days

with inner diameters ranging from 15 to 100 nm [175]. Cell adhesion, proliferation, and migration were significantly affected by the nanotube size. Clearly, geometries with a spacing of approximately 15 nm were most stimulating for cell growth and differentiation, whereas diameters of ~ 100 nm lead to a drastically increased cell apoptosis (see Fig. 15). This drastic effect of the nanoscale microenvironment on cell fate was ascribed to specific interactions between a specific nanotube size with the focal adhesion (FA) complex.

6.7 Other Aspects

Other applications of the tubes target H₂-sensing. For instance, Grimes et al. has shown manifold increase in electrical conductivity of the TiO₂ nanotube layer upon exposure to H₂ environments. For example, response in order of several magnitudes has been determined for 1000 ppm H₂ containing nitrogen atmospheres [176, 177].

For many applications, thin nanotubular layer of TiO₂ films on a foreign substrate is desired such as on Si-wafer or on conductive glass (ITO). Several groups reported successful fabrication of oxide nanotube layers from sputter-deposited thin titanium films [178–180]. The key is to alter the dissolution rate as much as possible, that is, to achieve high current efficiency (e.g., by lowering the electrolyte temperature).

The applications of TiO₂ nanotubes can significantly be expanded if secondary material can successfully be deposited into the tubes. Recently, such an approach has been reported that leads to selective electrodeposition of Cu into the tubes

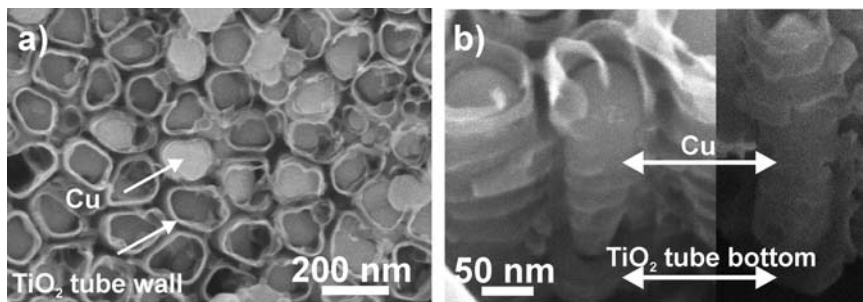


Fig. 16 SEM images showing top view (a) and cross-section (b) of nanotube layer with electrodeposited Cu filling the entire tube space

[181] leading to completely filled tubular layers (Fig. 16). This is an important step toward magnetic nanotube materials, solid-junction solar cells, or biomedical release systems.

References

1. H. Masuda, K. Fukuda, *Science* 268 (1995) 1466.
2. H. Masuda, K. Yada, A. Osaka, *Jap. J. Appl. Phys.* 37 (1998) L1340.
3. H. Masuda, K. Fukuda, *Appl. Phys. Lett.* 71 (1997) 2770.
4. O. Jessensky, F. Muller, U. Gösele, *Appl. Phys. Lett.* 72 (1998) 1173.
5. H. Masuda, K. Yada, A. Osaka, *Jap. J. Appl. Phys.* 38 (1999) L1403.
6. D. Al Mawiawi, N. Coombs, M. Moskovits, *J. App. Phys.* 70 (1991) 4421.
7. C. R. Martin, *Science* 266 (1994) 1961.
8. M. Steinhart, J. H. Wendorff, A. Greiner, R. B. Wehrspohn, K. Nielsch, J. Schilling, J. Choi, U. Gösele, *Science* 296 (2002) 1997.
9. V. Zwillling, E. Darque-Ceretti, A. Boutry-Forveille, *Electrochim. Acta* 45(1999) 921.
10. D. Gong, C. A. Grimes, O. K. Varghese, W. Hu, R. S. Singh, Z. Chen, E. C. Dickey, *J. Mater. Res.* 16 (2001) 3331.
11. R. Beranek, H. Hildebrand, P. Schmuki, *Electrochem. Solid-State Lett.* 6 (2003) B12.
12. J. M. Macak, K. Sirotna, P. Schmuki, *Electrochim. Acta* 50 (2005) 3679.
13. J. M. Macak, H. Tsuchiya, P. Schmuki, *Angew. Chem.* 44 (2005) 2100.
14. L. V. Taveira, J. M. Macak, H. Tsuchiya, L. F. P. Dick, P. Schmuki, *J. Electrochem. Soc.* 152 (2005) B405.
15. A. Ghicov, H. Tsuchiya, J. M. Macak, P. Schmuki, *Electrochem. Commun.* 7 (2005) 505.
16. J. M. Macak, H. Tsuchiya, L. Taveira, S. Aldabergerova, P. Schmuki, *Angew. Chem. Int. Ed.* 44 (2005) 7463.
17. P. Schmuki, H. Tsuchiya, L. V. Taveira, L. F. P. Dick, J. M. Macak, in *Proc. of the Symposium "Pits and Pores: Formation, Properties and Significance for Advanced Materials"*, P. Schmuki, D. J. Lockwood, H. S. Isaacs, Y. Ogata, M. Seo, Eds., The Electrochemical Society, PV of ECS Hawaii meeting 2004, PV 2004-19, 70.
18. H. Tsuchiya, P. Schmuki, *Electrochem. Commun.* 6 (2004) 1131.
19. H. Tsuchiya, J. M. Macak, I. Sieber, P. Schmuki, *Small* 1 (2005) 722.
20. W. J. Lee, W. H. Smyrl, *Electrochem. Solid-State Lett.* 8 (2005) B7.
21. I. Sieber, H. Hildebrand, A. Friedrich, P. Schmuki, *Electrochem. Commun.* 7 (2005) 97.
22. H. Tsuchiya, J. M. Macak, I. Sieber, L. Taveira, A. Ghicov, K. Sirotna, P. Schmuki, *Electrochem. Commun.* 7 (2005) 295.

23. N. Mukherjee, M. Paulose, O. K. Varghese, G. K. Mor, C. A. Grimes, *J. Mater. Res.* 18 (2003) 2296.
24. I. Sieber, B. Kannan, P. Schmuki, *Electrochem. Solid-State Lett.* 8 (2005) J10.
25. I. Sieber, P. Schmuki, *J. Electrochem. Soc.* 152 (2005) C639.
26. H. Tsuchiya, P. Schmuki, *Electrochem. Commun.* 7 (2005) 49.
27. A. Fujishima, K. Honda, *Nature* 238 (1972) 37
28. B. O'Regan, M. Grätzel, *Nature* 353 (1991) 737.
29. G. Sberveglieri Ed., *Gas Sensors*, Kluwer Academic Publishing, Dordrecht, 1992.
30. C. K. Dyer, J. S. L. Leach, *J. Electrochem. Soc.* 125 (1978) 1032.
31. J. W. Schultze, M. M. Lohrengel, D. Ross, *Electrochim. Acta* 28, (1983) 973.
32. P. Schmuki, *J. Solid State Electrochem.* 6 (2002) 145.
33. J. C. Marchenoir, J. P. Loup, J. Masson, *Thin Solid Films* 66 (1980) 357.
34. L. Arsov, M. Froehlicher, M. Froment, A. Hugot-le-Goff, *Journal de Chimie Physique* 3 (1975) 275.
35. G. Blondeau, M. Froehlicher, M. Froment, A. Hugot-le-Goff, *Journal de Microscopie et de spectroscopie electronique* 2 (1977) 27.
36. J. Yahalom, J. Zahavi, *Electrochim. Acta* 15 (1970) 1429.
37. J.-C. Marchenoir, J. Gautron, J. P. Loup, *Metaux, corrosion-industrie* (1977) 83.
38. J.-L. Delplancke, R. Winand, *Electrochim. Acta* 33 (1988) 1551.
39. S. R. Morrison, *Electrochemistry at semiconductor and oxidized metal electrodes*, Plenum Press, New York (1980).
40. S. M. Sze, *VLSI Technology*, McGraw-Hill, New York (1983).
41. S. Ikonopisov, *Electrochim. Acta* 22 (1977) 1077.
42. S. Ikonopisov, A. Girginov, M. Machkova, *Electrochimica Acta* 24 (1979) 451.
43. I. Montero, J. M. Albella, J. M. Martinez-Duart, *J. Electrochem. Soc.* 132 (1985) 814.
44. G. C. Wood, C. Pearson, *Corros. Sci.* 7 (1967) 119.
45. Y. T. Sul, C. B. Johansson, S. Petronis, A. Krozer, Y. Jeong, A. Wennerberg, T. Albrektsson, *Biomaterials* 23 (2002) 491.
46. Y. Mueller, S. Virtanen, in *Pits and Pores II*, P. Schmuki, D. J. Lockwood, Y. H. Ogata, H. S. Isaacs, Eds., *The Electrochemical Society Proceedings Series*, Pennington, NJ (2000), PV 2000-25, p. 294.
47. C. K. Dyer, J. S. L. Leach, *J. Electrochem. Soc.* 125 (1978) 23.
48. Z. Tun, J. J. Noel, D. W. Shoesmith, *J. Electrochem. Soc.* 146 (1999) 988.
49. P. F. Schmidt, *J. Appl. Phys.* 28 (1957) 278.
50. P. F. Schmidt, *J. Electrochem. Soc.* 115 (1968) 167.
51. D. A. Vermilyea, *J. Appl. Phys.* 27 (1956) 963.
52. A. Ward, A. Damjanovic, E. Gray, M. O'Jea, *J. Electrochem. Soc.* 123 (1976) 1599.
53. H. Böhni, PhD thesis 4020, ETH Zürich, 1967.
54. A. Singh, J. M. Macak, H. Hildebrand, P. Schmuki, in preparation.
55. V. P. Parkhutik, V. I. Shershulsky, *J. Phys. D.* 25 (1992) 1258.
56. V. Parkutik, *Pits and Pores II*, Proc. Vol. ECS 2000-25, (2000) 168.
57. K. Yasuda, P. Schmuki, *Electrochimica Acta* 52 (2007) 4053.
58. K. Yasuda, P. Schmuki, *Electrochem. Commun.* 9 (2007) 615.
59. X. Feng, J. M. Macak, P. Schmuki, *Chem. Mater.* 19 (2007) 1534.
60. S. Bauer, S. Kleber, P. Schmuki, *Electrochem. Commun.* 8 (2006) 1321.
61. J. M. Macak, P. Schmuki, *Electrochimica Acta* 52 (2006) 1258.
62. H. Tsuchiya, J. M. Macak, L. Taveira, E. Balaur, A. Ghicov, K. Sirotna, P. Schmuki, *Electrochem. Commun.* 7 (2005) 576.
63. S. Albu, A. Ghicov, J. M. Macak, P. Schmuki, *Phys. Stat. Sol. (RRL)* 1 (2007) R65
64. J. M. Macak, S. Albu, D. H. Kim, I. Paramasivam, S. Aldabergerova, P. Schmuki, *Electrochem. Solid-State Lett.*, 10(2007)K28.
65. S. Albu, A. Ghicov, J. M. Macak, R. Hahn, P. Schmuki, *Nano Lett.*, 7(2007)1286.
66. U. Ciesla, M. Froba, G. Stucky, F. Schüth, *Chem. Mater.* 11 (1999) 227.

67. B. T. Holland, C. F. Blanford, T. Do, A. Stein, *Chem. Mater.* 11 (1999) 795.
68. H.-R. Chen, J.-L. Shi, J. Yu, L.-Z. Wang, D.-S. Yan, *Micropor. Mesopor. Mater.* 39 (2000) 171.
69. P. Stefanov, D. Stoychev, M. Stoycheva, J. Ikonov, Ts. Marinova, *Surf. Interface Anal.* 30 (2000) 628.
70. R. A. Ploc, M. A. Miller, *J. Nucl. Mat.* 64 (1977) 71.
71. B. Cox, *J. Electrochem. Soc.* 117 (1970) 654.
72. M. Ohtaki, J. Peng, K. Eguchi, H. Arai, *Sens. Actuat. B* 13–14 (1993) 495.
73. G. H. Hutchings, S. H. Taylor, *Catal. Today* 49 (1999) 105.
74. R. I. Aagard, *Appl. Phys. Lett.* 27 (1975) 605.
75. B. Ohtani, K. Iwai, S. Nishimoto, T. Inui, *J. Electrochem. Soc.* 141 (1994) 2439.
76. J. Choi, J. H. Lim, S. Ch. Lee, J. H. Chang, K. J. Kim, M. A. Cho, *Electrochimica Acta* 51 (2006) 5502.
77. J. Choi, J. H. Lim, J. Lee, K. J. Kim, *Nanotechnology* 18 (2007) 055603.
78. R. Karlinsky, *Electrochem. Commun.* 7 (2005) 1190.
79. Y. Masuda, S. Wakamatsu, K. Koumoto, *J. European Ceram. Soc.* 24 (2004) 301.
80. K. Kamada, M. Mukai, Y. Matsumoto, *Electrochimica Acta* 49 (2004) 321.
81. A. Mozalev, M. Sakairi, I. Saeki, H. Takahashi, *Electrochimica Acta* 48 (2003) 3155.
82. A. I. Vorobyova, E. A. Outkina, *Thin Solid Films* 324 (1998) 1.
83. W. S. Kim, J. H. Kim, J. H. Kim, K. H. Hur, J. Y. Lee, *Mater. Chem.* 79 (2003) 204.
84. C. Wang, L. Fang, G. Zhang, D. M. Zhuang, M. S. Wu, *Thin Solid Films* 458 (2003) 246.
85. M. A. Butler, R. D. Nasby, R. K. Quinn, *Solid State Commun.* 19 (1976) 1011.
86. A. E. Aliev, H. W. Shin, *Solid State Ionics* 154–155 (2002) 425.
87. S. Badilescu, P. V. Ashrit, *Solid State Ionics* 158 (2003) 187.
88. E. Ozkan, S.-H. Lee, P. Liu, C. E. Tracy, F. Z. Tepehan, J. R. Pitts, S. K. Deb, *Solid State Ionics* 149 (2002) 139.
89. Y.-K. Chung, M.-H. Kim, W.-S. Um, H.-S. Lee, J.-K. Song, S.-C. Choi, K.-M. Yi, M.-J. Lee, K.-W. Chung, *Sensor. Actuator. B* 60 (1999) 49.
90. C. Cantalini, M. Pelino, H.-T. Sun, M. Faccio, S. Santucci, L. Lozzi, M. Passacantando, *Sensor. Actuator. B* 35–36 (1996) 112.
91. H.-T. Sun, C. Cantalini, L. Lozzi, M. Passacantando, S. Santucci, M. Pelino, *Thin Solid Films* 287 (1996) 258.
92. M. Tong, G. Dai, Y. Wu, X. He, D. Gao, *J. Mater. Sci.* 36 (2001) 2535.
93. B. Reidhman, A. J. Bard, *J. Electrochem. Soc.* 126 (1979) 583.
94. M.-G. Verge, C.-O. A. Olsson, D. Landolt, *Corros. Sci.* 46 (2004).
95. S. Berger, H. Tsuchiya, A. Ghicov, P. Schmuki, *Appl. Phys. Lett.* 88 (2006) 203119.
96. V. Zwillig, E. Darque-Ceretti, A. Boutry-Forveille, D. David, M. Y. Perrin, M. Aucouturier, *Surf. Interface Anal.* 27 (1999) 629.
97. J. M. Macak, H. Tsuchiya, L. Taveira, A. Ghicov, P. Schmuki, *J. Biomed. Mat. Res.* 75A (2005) 928.
98. H. Tsuchiya, J. M. Macak, A. Ghicov, P. Schmuki, *Small* 2 (2006) 888.
99. H. Tsuchiya, J. M. Macak, A. Ghicov, Y. Ch. Tang, S. Fujimoto, M. Niinomi, T. Noda, P. Schmuki, *Electrochimica Acta* 52 (2006) 94.
100. A. Ghicov, S. Aldabergerova, P. Schmuki, *Angew. Chem. Int. Ed.* 44 (2005) 7463.
101. O. K. Varghese, D. Gong, M. Paulose, C. A. Grimes, E. C. Dickey, *J. Mater. Res.* 18 (2003) 156.
102. A. Ghicov, M. Yamamoto, P. Schmuki, *Angew. Chem. Int. Ed.* 47(2008) 7934.
103. K. Yasuda, P. Schmuki, *Adv. Mater.*, 19 (2007) 1757.
104. K. Wakino, K. Minai, H. Tamura, *J. Am. Ceram. Soc.* 36 (1984) 278.
105. C. L. Wang, H. Y. Lee, F. Azough, R. Freer, *J. Mater. Sci.* 32 (1997) 1693.
106. A. Bianco, G. Gusmano, R. Freer, P. Smith, *J. Eur. Ceram. Soc.* 19 (1999) 959.
107. D.-A. Chang, P. Lin, T. Tseng, *J. Appl. Phys.* 77 (1995) 4445.
108. X. Z. Fu, L. A. Clark, Q. Yang, M. A. Anderson, *Environ. Sci. Technol.* 30 (1996) 647.

109. F. H. Simpson, *Mater. Eng.* 52 (1960) 16.
110. D. Kuroda, M. Niinomi, M. Morinaga, Y. Kato, T. Yashiro, *Mater. Sci. Eng.* 1998, A243, 244.
111. H. Tsuchiya, S. Berger, J. M. Macak, A. G. Munoz, P. Schmuki, *Electrochem. Commun.* 9 (2007) 545.
112. M. Grätzel, *Nature* 414 (2001) 338.
113. A. L. Linsebigler, G. Lu, J. T. Yates, *Chem. Rev.* 95 (1995) 735.
114. A. Ghicov, H. Tsuchiya, J. M. Macak, P. Schmuki, *Phys. Stat. Sol. A* 203 (2006) R28.
115. J. Zhao, X. Wang, T. Sun, L. Li, *Nanotechnology* 16 (2005) 2450.
116. J. M. Macak, S. Aldabergerova, A. Ghicov, P. Schmuki, *Phys. Stat. Sol. A* 203 (2006) R67.
117. J. Arbiol, J. Cerda, G. Dezanneau, A. Cicera, F. Peiro, A. Cornet, J. R. Moraste, *J. Appl. Phys.* 92 (2002) 853.
118. B. Tryba, A. W. Moravski, M. Inagaki, *Appl. Catal. B: Environ.* 52 (2003) 203.
119. K. Shimizu, K. Kobayashi, *J. Surf. Finish. Soc. Jpn.* 46 (1995) 402.
120. J. Kunze, A. Ghicov, H. Hildebrandt, J. M. Macak, L. Taveira, P. Schmuki *Z. Phys. Chem.* 129 (2006) 1561.
121. J. Lausmaa, *J. Electron Spectrosc. Relat. Phenom.* 81 (1996) 343.
122. R. Beranek, H. Tsuchiya, T. Sugishima, J. M. Macak, L. Taveira, S. Fujimoto, H. Kisch, P. Schmuki, *Appl. Phys. Lett.* 87 (2005) 243114.
123. S. Tanemura, L. Miao, P. Jin, K. Kaneko, A. Terai, N. Nabatova-Gabain, *Appl. Surf. Sci.* 212–213 (2003) 654.
124. D. Mardare, G. I. Rusu, *Mater. Lett.* 56 (2002) 210.
125. J. M. Macak, H. Tsuchiya, A. Ghicov, P. Schmuki, *Electrochem. Commun.* 7 (2005) 1138.
126. R. Asahi, T. Morikawa, T. Ohwaki, A. Aoki, Y. Taga, *Science* 293 (2001) 269.
127. K. Wilke, H. D. Breuer, *J. Photochem. Photobiol., A* 127 (1999) 107.
128. L. Lin, W. Lin, Y. Zhu, B. Zhao, Y. Xie, *Chem. Lett.* 34 (2005) 284.
129. M. Anpo, *Catal. Surv. Jpn.* 1 (1997) 169.
130. T. Yamaki, T. Umebayashi, T. Sumita, S. Yamamoto, M. Maekawa, A. Kawasuso, H. Itoh, *Nucl. Instrum. Methods Phys. Res. Sec. B* 206 (2003) 254.
131. S. Sakthivel, H. Kisch, *Angew. Chem. Int. Ed.* 42 (2003) 4908.
132. T. Ohno, T. Mitsui, M. Matsumura, *Chem. Lett.* 32 (2003) 364.
133. T. Umebayashi, T. Yamaki, S. Tanaka, K. Asai, *Chem. Lett.* 32 (2003) 330.
134. W. Zhao, W. Ma, C. Chen, J. Zhao, Z. Shuai, *J. Am. Chem. Soc.* 126 (2004) 4782.
135. A. Ghicov, J. M. Macak, H. Tsuchiya, J. Kunze, V. Heublein, L. Frey, P. Schmuki, *Nano Lett.* 6 (2006) 1080.
136. A. Ghicov, J. M. Macak, H. Tsuchiya, J. Kunze, V. Haeublein, S. Kleber, P. Schmuki, *Chem. Phys. Lett.* 419 (2005) 426.
137. R. P. Vitiello, J. M. Macak, A. Ghicov, H. Tsuchiya, L. F. P. Dick, P. Schmuki, *Electrochem. Commun.* 8 (2006) 544.
138. J. M. Macak, A. Ghicov, R. Hahn, H. Tsuchiya, P. Schmuki, *J. Mater. Res.* 21 (2006) 2824.
139. K. Shankar, K. Ch. Tep, G. K. Mor, C. A. Grimes, *J. Phys. D: Appl. Phys.* 39 (2006) 2361.
140. A. Ghicov, B. Schmidt, J. Kunze, P. Schmuki, *Chem. Phys. Lett.* 433 (2007) 323.
141. J. H. Park, S. Kim, A. J. Bard, *Nanoletters* 6 (2006) 24.
142. R. Hahn, A. Ghicov, J. Salonen, P. Schmuki, *Nanotechnology* 18 (2007) 105604.
143. I. I. Philips, P. Poole, L. L. Shreir, *Corros. Sci.* 12 (1972) 855.
144. Z. A. Foroulis, *J. Electrochem. Soc.* 128 (1981) 219.
145. E. Brauer, R. Gruner, F. Rauch, *Ber. Bunsen. Phys. Chem.* 87 (1983) 341.
146. D. J. Blackwood, L. M. Peter, H. E. Bishop, P. R. Chalker, D. E. Williams, *Electrochim. Acta* 34 (1989) 1401.
147. H. Tokudome, M. Miyauchi, *Angew. Chem., Int. Ed.* 44 (2005) 1974.
148. A. Ghicov, H. Tsuchiya, R. Hahn, J. M. Macak, A. G. Munoz, P. Schmuki, *Electrochem. Commun.* 8 (2006) 528.
149. N. Sakai, A. Fujishima, T. Watanabe, K. Hashimoto, *J. Electrochem. Soc.* 148 (2001) E395.

150. R. Hahn, A. Ghicov, H. Tsuchiya, J. M. Macak, A. G. Munoz, P. Schmuki, *Phys. Stat. Sol. A* 204 (2007) 1281.
151. M. R. Hofmann, S. T. Martin, W. Choi, D. W. Bahnemann, *Chem. Rev.* 95 (1995) 69.
152. A. Mills, S. Le Hunte, *J. Photochem. Photobiol. A* 108 (1997) 1.
153. F. Kiriakidou, D. I. Kondarides, X. E. Verykios, *Catalysis Today* 54 (1999) 119.
154. F. Zhang, J. Zhao, T. Shen, H. Hidaka, E. Pelizzetti, N. Serpone, *Appl. Catal. B* 15 (1998) 147.
155. J. Krýsa, M. Keppert, G. Waldner, J. Jirkovský, *Electrochim. Acta* 50 (2005) 5255.
156. N. Serpone, E. Pelizzetti, *Photocatalysis – Fundamentals and Applications*, Wiley, New York, 1989.
157. D. F. Ollis, H. Al-Ekabi, *Photocatalytic Purification and Treatment of Water and Air*, Elsevier, Amsterdam, (1993).
158. J. M. Macak, M. Zlamal, J. Krysa, P. Schmuki, *Small* 3 (2007) 303.
159. E. Balaur, J. M. Macak, L. Taviera, H. Tsuchiya, P. Schmuki, *Electrochem. Commun.* 7 (2005) 1066.
160. E. Balaur, J. M. Macak, H. Tsuchiya, P. Schmuki, *J. Mater. Chem.* 15 (2005) 4488.
161. R. Wang, K. Hashimoto, A. Fujishima, M. Chikuni, E. Kojima, A. Kitamura, M. Shimohigoshi, T. Watanabe, *Nature* 388 (1997) 431.
162. R. Wang, K. Hashimoto, A. Fujishima, M. Chikuni, E. Kojima, A. Kitamura, M. Shimohigoshi, T. Watanabe, *Adv. Mater.* 10 (1998) 135.
163. J. P. Lee, H. K. Kim, C. R. Park, G. Park, H. T. Kwak, S. M. Koo, M. M. Sung, *J. Phys. Chem. B* 107 (2003) 8997.
164. J. P. Lee, H. K. Kim, C. R. Park, G. Park, H. T. Kwak, S. M. Koo, M. M. Sung, *J. Phys. Chem. B* 107 (2003) 8997.
165. D. M. Brunette, P. Tengvall, M. Textor, P. Thomsen, *Titanium in Medicine*. Springer, Berlin (2001).
166. X. Liu, P. K. Chu, C. Ding, *Mater. Sci. Eng. R* 47 (2004) 49.
167. C. M. Roome, C. D. Adam, *Biomaterials* 16 (1995) 69.
168. J. Weng, Q. Liu, J. G. C. Wolke, X. Zhang, K. de Groot, *Biomaterials* 18 (1997) 1027.
169. P. Li, C. Ohtsuki, T. Kokubo, K. Nakanishi, N. Soga, K. de Groot, *J. Biomed. Mater. Res.* 28 (1994) 7.
170. P. Li, I. Kangasniemi, K. de Groot, T. Kokubo, *J. Am. Ceram. Soc.* 5 (1994) 1307.
171. L. Jonasova, F. A. Müller, A. Helebrant, J. Strnad, P. Greil, *Biomaterials* 23 (2002) 3095.
172. B. Yang, M. Uchida, H. M. Kim, X. Zhang, T. Kokubo, *Biomaterials* 25 (2004) 1003.
173. W. H. Song, Y. K. Jun, Y. Han, S. H. Hong, *Biomaterials* 25 (2004) 3341.
174. H. Tsuchiya, J. M. Macak, L. Muller, J. Kunze, F. Muller, S. P. Greil, S. Virtanen, P. Schmuki, *J. Biomed. Mat. Res.* 2006, 77A, 534.
175. J. H. Park, S. Bauer, K. von der Mark, P. Schmuki, *Nano Lett.* 7 (2007) 1686.
176. O. K. Varghese, D. Gong, K. G. Ong, C. A. Grimes, *Sensors and Actuators B* 93, (2003) 338.
177. O. K. Varghese, D. Gong, M. Paulose, K. G. Ong, E. C. Dickey, C. A. Grimes, *Adv. Mater.* 15 (2003) 624.
178. J. M. Macak, H. Tsuchia, S. Berger, S. Bauer, S. Fujimoto, P. Schmuki *Chem. Phys. Lett.* 428 (2006) 421.
179. X. Yu, Y. Li, W. Ge, Q. Yang, N. Zhu, K. K. Zadeh, *Nanotechnology* 17 (2006) 808.
180. Y. D. Premchand, T. Djenizian, F. Vacandio, P. Knauth, *Electrochem. Commun.* 8 (2005) 1840.
181. J. M. Macak, B. G. Gong, M. Hueppe, P. Schmuki, *Adv. Mater.* 19 (2007) 3027.